Helium mediated deposition: Modeling the He−TiO2(110)-(1×1) interaction potential and application to the collision of a helium droplet from density functional calculations

Néstor F. Aguirre, David Mateo, Alexander O. Mitrushchenkov, Martí Pi, and María Pilar de Lara-Castells

Citation: J. Chem. Phys. **136**, 124703 (2012); doi: 10.1063/1.3698173
View online: http://dx.doi.org/10.1063/1.3698173
View Table of Contents: http://jcp.aip.org/resource/1/JCPSA6/v136/i12
Published by the American Institute of Physics.

Helium mediated deposition: Modeling the He−TiO_2(110)-(1×1) interaction potential and application to the collision of a helium droplet from density functional calculations

Néstor F. Aguirre,[1] David Mateo,[2] Alexander O. Mitrushchenkov,[3] Martí Pi,[2] and María Pilar de Lara-Castells[1,a)]

[1]*Instituto de Física Fundamental (C.S.I.C.), Serrano 123, E-28006 Madrid, Spain*
[2]*Departament ECM, Facultat de Física, and IN²UB, Universitat de Barcelona, Diagonal 647, 08028 Barcelona, Spain*
[3]*Université Paris-Est, Laboratoire Modélisation et Simulation Multi Echelle, MSME UMR 8208 CNRS, 5 bd Descartes, 77454 Marne-la-Vallée, France*

(Received 2 January 2012; accepted 5 March 2012; published online 29 March 2012)

This paper is the first of a two-part series dealing with quantum-mechanical (density-functional-based) studies of helium-mediated deposition of catalytic species on the rutile TiO_2(110)-(1×1) surface. The interaction of helium with the TiO_2(110)-(1×1) surface is first evaluated using the Perdew-Burke-Ernzerhof functional at a numerical grid dense enough to build an analytical three-dimensional potential energy surface. Three (two prototype) potential models for the He-surface interaction in helium scattering calculations are analyzed to build the analytical potential energy surface: (1) the hard-corrugated-wall potential model; (2) the corrugated-Morse potential model; and (3) the three-dimensional Morse potential model. Different model potentials are then used to study the dynamics upon collision of a $^4He_{300}$ cluster with the TiO_2(110) surface at zero temperature within the framework of a time-dependent density-functional approach for the quantum fluid [D. Mateo, D. Jin, M. Barranco, and M. Pi, J. Chem. Phys. **134**, 044507 (2011)] and classical dynamics calculations. The laterally averaged density functional theory-based potential with an added long-range dispersion interaction term is further applied. At variance with classical dynamics calculations, showing helium droplet splashing out of the surface at impact, the time evolution of the macroscopic helium wavefunction predicts that the helium droplet spreads on the rutile surface and leads to the formation of a thin film above the substrate. This work thus provides a basis for simulating helium mediated deposition of metallic clusters embedded within helium nanodroplets. © *2012 American Institute of Physics*. [http://dx.doi.org/10.1063/1.3698173]

I. INTRODUCTION

The analysis of wetting and spreading properties of quantal fluids (e.g., helium or *para*-hydrogen films) adsorbed on different substrates has stimulated much experimental and theoretical work during the last years (see, for example, Refs. 1–4). Besides obtaining a better microscopic understanding of the fundamental physics upon collision of a quantal fluid with a surface, the fruitful application of helium nanodroplets to the soft-landing deposition of catalytic species (e.g., metallic nano-clusters) immersed within the drop on the surface of different substrates[5–7] has provided a renewed impetus for further theoretical works.

Soft-landing (SL) techniques (see, e.g., Ref. 8 for a recent review) were already described in the seventies and proposed as a tool to prepare modified surfaces by Cooks and co-workers.[9] Two decades later, the same group applied the method to achieve the intact deposition of mass-selected ionized species onto self-assembled mono-layer surfaces.[10] Further studies showed that the method allows the intact deposition of complex ions such as peptides and proteins on different substrates (see, e.g., Ref. 11). Nowadays, rapid development in the fields of nano-science and nano-technology has raised new challenges in the application of SL techniques as, for example, in the controlled synthesis and characterization of nano-structured metal/oxide catalysts.[12–14] In fact, re-structuring of metallic nano-particles upon adsorption on the supported oxide (i.e., fragmenting and/or sintering after deposition) can alter their targeted size-dependent catalytic properties,[15] making the development of SL techniques an important research goal.[16] Recent experimental studies carried out by Vilesov and co-workers[7] have shown that helium nanodroplets serve not only as a gentle matrix where metallic clusters tailored in size are formed but also as carriers to the surface of a substrate at very low landing energies (below 0.1 eV per atom[7]). The realization of SL conditions in which the embedded species sticks the surface, with a probability near unity,[6] keeping its identity[17] was indirectly proven by the similar size-distribution of the metallic clusters within the droplet and after deposition on the substrate, according to the images obtained by transmission electron microscopy.[7]

Despite these important recent progress on helium-mediated deposition techniques,[6,7] little is known about the microscopic mechanism that renders the soft-landing of the

a)E-mail: Pilar.deLara.Castells@csic.es.

embedded metal cluster possible. The evolution of the droplet carrier itself upon collision (i.e., with wetting, rebounding, spreading or splashing as possible outcomes) and characteristic time-scales play a crucial role in pre-conditioning the metallic cluster deposition process. This study is aimed at providing basic understanding on the collision of the helium droplet carrier with a surface, choosing a prototype metal-oxide as the substrate.

In recent years, a few first-principle molecular dynamics simulations on the soft-landing of metal clusters (e.g., Pd clusters) onto oxide surfaces have been carried out by, for example, Landman and co-workers (see, e.g., Ref. 18). These studies revealed that metal clusters retain their gas-phase structures at low impact energies of 0.1 eV per atom. In contrast with the nuclear dynamics of heavy metal atoms, a proper description of the helium droplet must consider its quantum nature, specially at the low droplet temperature in the experimental measurements.[6,7] A time-dependent density-functional-theory (TDDFT) description of the helium droplet has proved to be an efficient, computationally feasible and robust approach to study different dynamical processes in helium droplets such as the photo-desorption of alkali atoms,[19] or the evolution of electron-bubble states.[20] We apply this approach here to model the collision dynamics of a helium drop with a metal-oxide surface with the initial conditions chosen to resemble those described in the experimental setup.[7]

As a technological relevant system in photo-electronics and heterogeneous catalysis and photo-catalysis[21–23] and a prototype metal-oxide substrate with well-characterized properties[21] we have chosen the perfect rutile TiO_2 (110)-(1×1) surface. This selection is also motivated by the fact that nano-sized particles of noble metals adsorbed on TiO_2-based surfaces play a key role in improving the catalytic and photo-catalytic properties of the substrate,[24] allowing the formation of new active sites and facilitating a more efficient separation and diffusion of photo-generated electron-hole pairs.[25]

A prerequisite for these dynamical studies is the availability of a realistic potential energy surface (PES). By resorting to the pairwise approach, the global PES is expressed as a sum of N He$-TiO_2$ plus the He-He potential energy terms. Whereas the ground-state He$-$He interaction potential is well-characterized (see, e.g., Ref. 26 and references therein) we are aware of only one first-principle study on the He-TiO_2(110)-(1×1) interaction.[27] This recent study has shown that periodic calculations using the Perdew-Burke-Ernzerhof (PBE) functional and an electronic basis set tailored to minimize the basis set superposition error, yield a short and medium-range interaction potential, as a function of the vertical height z above the most stable adsorption site, in very reasonable agreement with those obtained using correlated wave-function-based methods and finite, hydrogen-terminated and embedded, model cluster approaches. In particular, the well-depth (84 cm^{-1}) and the equilibrium distance (3.2 Å) obtained through periodic PBE calculations underestimated by less than 2% and 5%, respectively, the values evaluated at local Möller-Plesset second order perturbation (LMP2) level on the largest hydrogen-terminated cluster considered (of stoichiometry $Ti_9O_{34}H_{32}$). Likewise, the correlation energies calculated with a modified version[28] of the cluster-in-solid embedding technique[29] agreed with those obtained with a similar size hydrogen-terminated cluster within 10%, indicating the validity of the adopted hydrogen-saturated cluster models.[27] On the other hand, MP2 correlation energies calculated with the embedded cluster approach underestimated those evaluated using the more accurate coupled cluster theory through perturbative triples, CCSD(T), by less than 15%. Benchmark periodic MP2 calculations with the CRYSCOR code[30] on the He$-$MgO(100) interaction by Martinez-Casado *et al.*[31] also revealed a good agreement between PBE and MP2 results for the well-depth (to within 0.3 meV). Similarly to the case of the He$-TiO_2$(110) interaction,[27] these results showed the inability of the PBE approach to describe the long-range dispersive interaction and then the proper $-1/z^3$ asymptotic behaviour. This arises from the well-known fundamental problem of local and semilocal DFT functionals to capture the correct $1/R^6$ dependence of the dispersion energy as a function of the distance R between the interacting fragments (see, e.g., for recent reviews Refs. 32 and 33).

Due to the lack of long-range dispersion correlation, the ability of the PBE approach to perform reasonably in weakly bound systems (e.g., water-metal interfaces[34]) has been attributed to overbinding effects in the water-water interaction compensating for the missing dispersion contribution.[35,36] Besides compensating effects, a localized molecular orbital energy decomposition analysis combined with symmetry adapted perturbation theory (SAPT) by Jordan and co-workers[37] disclosed the recovery of short-range dispersion effects (i.e, defined in the framework of SAPT) in DFT calculations of water clusters. Unraveling such effects in PBE calculations of the He$-TiO_2$ interaction would benefit from such decomposition studies by using model cluster approaches. Given the lack of any experimental study giving insight into the characteristics of the He$-TiO_2$(110)-(1×1) interaction or higher level *ab initio* calculations to compare with, we consider our periodic PBE approach as sensible for the calculation of the short- and medium-range region of the full, three-dimensional, He$-TiO_2$(110)-(1×1) PES. On the other hand, the exact form of the long-range tail is not expected to affect strongly the collision dynamics due to the high velocities of the helium nanodrop in the experimental measurements (about 200 m/s from Ref. 7). With the aim of assessing it, we also considered a model potential which includes a long-range correction term in the dynamics calculations. Moreover, additional calculations are presented by using the van der Waals density functional (vdW-DF) of Langreth and co-workers.[38]

The periodic DFT calculations reported in Ref. 27 were restricted to the potential regions falling around the minimum energy path. We have performed additional calculations on a dense three-dimensional grid to provide the necessary data for the fitting of the global He-surface PES. Specifically, three models of increasing complexity have been chosen so that the adjustable parameters have a clear physical interpretation: (1) the hard-corrugated-wall (HCW) potential model; (2) the corrugated-Morse (CM) potential model; and (3) a three-dimensional Morse (3DM) potential model. The HCW and CM models are commonly used for first-principle simulations on the diffraction of atomic helium beams from

metal and metal-oxide surfaces (see., e.g., Ref. 39). Although such simulations are beyond the scope of our work, we also present the fitted parameters of these model potentials with the aim of providing some guidance on first-principle simulations of helium atom diffraction. The TDDFT simulation of the helium droplet dynamics in collisions with the $TiO_2(110)$-(1×1) surface has been carried out with a cluster composed by 300 helium atoms. Although this cluster size is much smaller than the average sizes formed through the experimental setup[7] (i.e., nanodroplets with more than 10^6 He atoms), it is considered large enough to provide meaningful physical insight into the process and, at the same time, keeping the computational calculation feasible. Pioneering TDDFT simulations of ^{4}He nanodroplets interacting with (weakly) attractive alkali metal surfaces were carried out by Giacomazzi *et al.*[1] As far as we are aware, our work represents the first study considering the case of a metal-oxide surface. With a well-depth more than an order of magnitude larger than in the case of alkali metal surfaces (10 vs. 0.6 meV for a Cs surface from Ref. 40) the $TiO_2(110)$ surface can be considered as representative of a stronger adsorber.

Section II provides the details on the construction of the He@$TiO_2(110)$-(1×1) potential energy surface, including the analysis of the different potential models, considering the inclusion of long-range dispersion corrections, and testing the validity of the pairwise additive approach in the case of two He atoms interacting with the surface. A very brief outline of the TDDFT method and the analysis of its application to the collision dynamics of a $^4He_{300}$ cluster impinging the He−$TiO_2(110)$-(1×1) surface are provided in Sec. III. The classical dynamics calculations are also presented in this section. The last section closes with a summary of the results and some final remarks. Additional details of our work are provided in the supplementary material.[41]

II. HE@TIO$_2$(110)-(1 × 1) POTENTIAL ENERGY SURFACE

The details of the computational setup have been presented in a previous study[27] so we give just a brief description here. The computations were performed with the CRYSTAL 09 code,[42] employing the PBE form[43] of the generalized gradient approximation with an all-electron basis set and Bloch functions defined as linear combinations of atom-centered Gaussian-type functions. The basis set was specifically tailored to minimize the basis set superposition error.[27] The $TiO_2(110)$-(1×1) surface was represented by the slab shown in Fig. 1. It consists of five molecular layers and a (3×1) surface unit cell (i.e., triple in the [001] direction and single in the $[\bar{1}10]$ direction, see Fig. 1). The Brillouin-zone integrations were carried out with a Monkhorst-Pack grid[44] using a shrinking parameter IS = 6.[42] Two helium atoms were

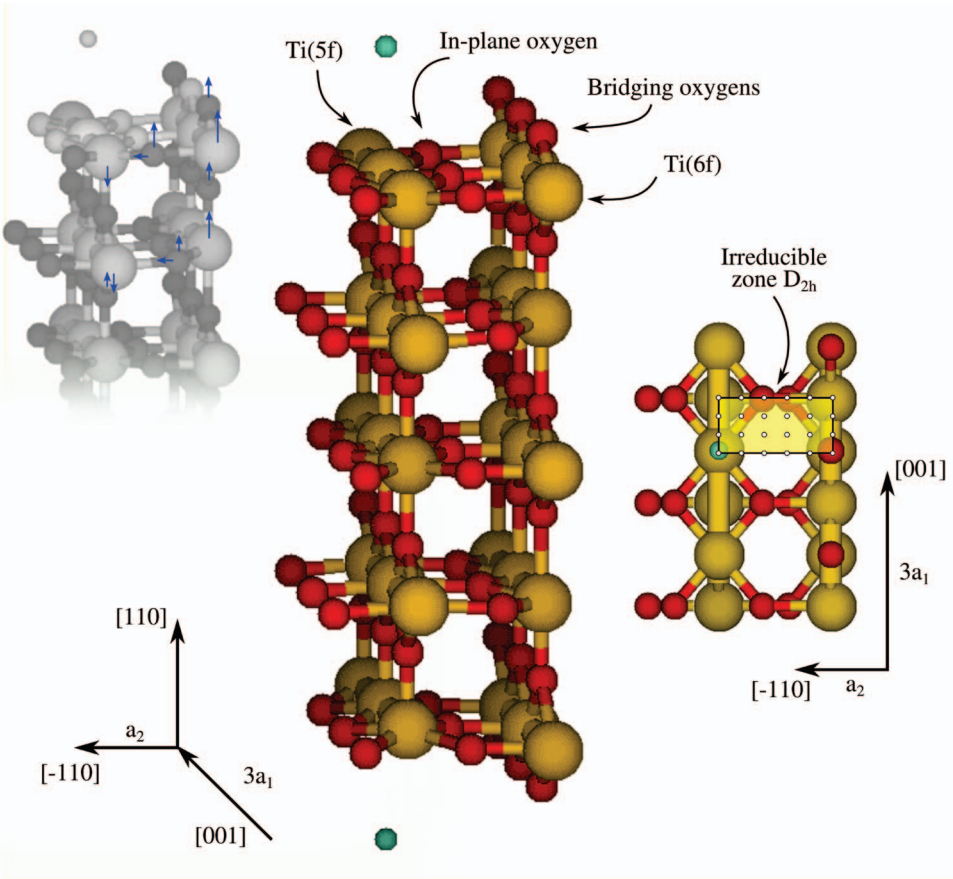

FIG. 1. Ball-and-stick representation of the 3 × 1 supercell slab model used to represent the rutile $TiO_2(110)$-(1×1) surface. The highlighted area defines the irreducible zone if a D_{2h} symmetry is imposed for the first molecular layer. Titanium (oxygen) atoms are highlighted in yellow (red). Green color spheres denote the adsorbed He atoms. The lattice vectors and atomic displacements from bulk-terminated positions are also indicated.

then placed on both sides of the slab so that the symmetry is higher. Since the He−He interaction decays very rapidly at large distances, this is justified. The slab geometry was frozen to experimental-based atomic positions (see below). As also mentioned in Ref. 27, the frozen slab approach is justified by the fact that only minor surface ion displacements were observed upon helium physisorption (0.0013 Å as much).

The surface exposes two types of titanium atoms, 5-fold coordinated Ti(5*f*) and 6-fold coordinated Ti(6*f*), and two types of oxygen atoms: 2-fold coordinated protruding O atoms (bridging oxygen) and 3-fold coordinated in-plane O atom (basal oxygen). The ideal bulk-terminated TiO_2(110) surface, with lattice constants $a = b = 4.593$ Å and $c = 2.985$ Å from Ref. 45, has adjacent bridging oxygen rows separated by $a_1 = 6.495$ Å and elevated by about 1.2 Å with respect to the basal plane, and bridging oxygen atoms within the same row separated by $a_2 = 2.985$ Å, with a_1 and a_2 denoting the surface lattice constants. In the relaxed TiO_2 (110)-(1×1) surface, the atomic positions are considerably displaced as compared with ideal bulk-terminated positions. According to a very recent analysis of low-energy electron-diffraction and surface x-ray diffraction data obtained from the TiO_2(110)-(1×1) surface,[46] the Ti(5*f*) atoms beneath the basal plane by 0.11 ± 0.01 Å whereas the bridging oxygen atoms experience a vertical displacement away from the bulk of 0.10 ± 0.04 Å (see also Fig. 1). As a result, the bridging oxygen atoms protrude by ∼1.5 Å from the Ti(5*f*)-surface plane. The atomic positions within the slab were fixed to these experimental-based values.[46]

The Cartesian coordinate axes were defined in such a way that *x*, *y*, and *z* correspond to the [001], [$\bar{1}$10], and [110] crystallographic directions with the origin at the deepest atomic site in the basal plane (the Ti(5*f*) site). The sampling of the three-dimensional $V(x, y, z)$ PES was obtained by choosing the helium lateral positions (x, y) on an equally spaced grid 4 × 6 within the asymmetric cell with $\Delta x = 0.50$ and $\Delta y = 0.65$ Å as shown in Fig. 1. The *z* grid associated to each lateral position (x, y) was composed by an average of 20 unequally spaced points with a Δz spacing between 0.1 and 0.5 Å. This *z*-grid was calibrated to ensure a smooth profile of the potential energy curves $V(z)$ obtained by cubic interpolation with a Δz spacing of 0.1 Å.

Figure 2 shows contour plots of the PES for four different *z* values. As discussed in Ref. 27, the global minimum is located on top of the Ti(5*f*) site with an equilibrium He−Ti(5*f*) distance of 3.2 Å and a well-depth of 83.6 cm^{-1}. On the other hand, the PES has a saddles (local minima) on top of the bridging oxygen atoms, at a vertical distance of about 4.7 Å from the Ti(5*f*)-plane, the three-fold coordinated oxygen atoms, and the Ti(6*f*) sites. The equilibrium vertical distances of the interaction potentials upon adsorption of a helium atom on top of Ti(5*f*) and bridging oxygen sites differ by about 1.5 Å. This is the same value obtained for the vertical distance between the Ti(5*f*) and the protruding oxygen atoms which is related to the surface corrugation along the [$\bar{1}$10] direction. We adopt the term *potential corrugation* here as the energy difference ΔV between the potential at the atomic *hills* (located at the bridging oxygen sites) and the atomic *valleys* (defined as the locations of the Ti(5*f*) sites) on the basal plane. The *z*-dependence of the absolute value of ΔV on a logarithmic scale is depicted in the lower panel of Fig. 2. Both the potential contours and $\Delta V(z)$ show the so-called potential *anti-corrugation*. At large *z* distances, the minima are located at the protruding oxygen atoms, ΔV is negative, and the

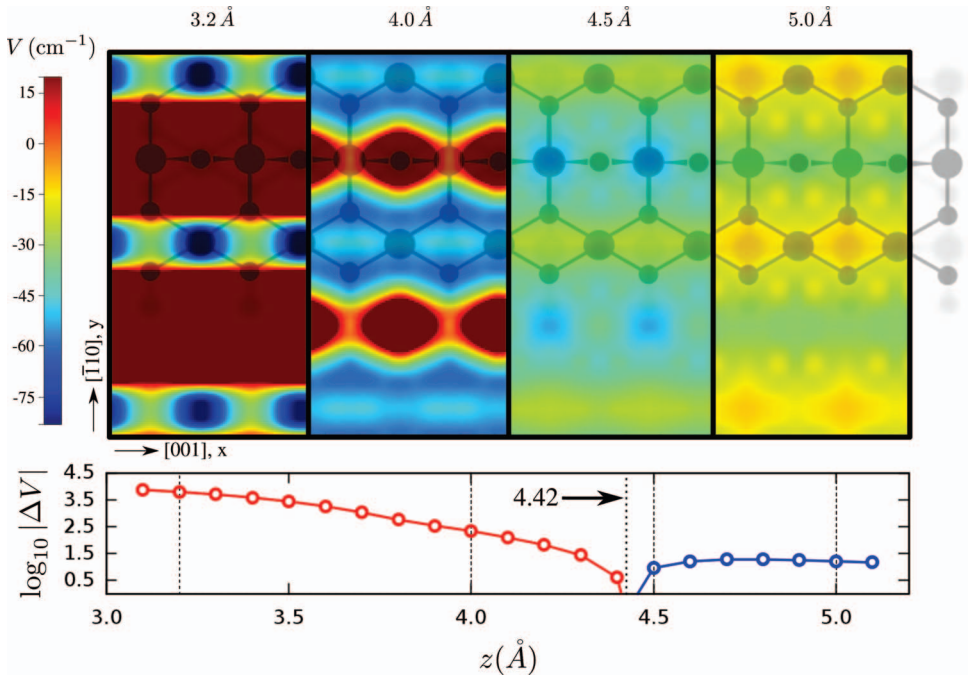

FIG. 2. Upper panel: Contour plots of the He-TiO_2(110)-(1×1) potential energy surface for four different vertical distances between the helium atom and the surface, taking the position of the Ti(5*f*) atom as zero. The atoms exposed on the surface are shown to guide the eye. Lower panel: *z*-dependence associated to the absolute value of the energy difference ΔV between the potential interaction with a helium atom sitting on the bridging oxygen atom and located on top the Ti(5*f*) sites.

potential is thus anti-corrugated. At closer vertical distances, however, the opposite trend is observed and the potential becomes corrugated (minima at the Ti(5*f*) sites and a positive value of ΔV). In the asymptotic limit, ΔV is negligible (i.e., about -0.01 cm^{-1} at $z = 15$ Å). As the helium atom approaches the surface the (negative) value of ΔV increases (see the lower panel of Fig. 2). Then, at $z \sim 4.8$ Å, the ΔV value starts to decrease, becoming equal to zero at $z = 4.42$ Å (see Fig. 2) and reverting its sign closely to the Ti(5*f*)-surface plane. This effect has been also found in the case of different rare-gas atoms interacting with metal surfaces (see., e.g., Ref. 47). The existence of a vertical atom-surface distance for which the potential corrugation equals to zero has suggested the existence of a *super-lubricity* state at some pressure value for sliding rare-gas mono-layers on metal surfaces.[47] All the calculated DFT-PBE energies are available on request from the authors.

A. Parameterization of the three-dimensional potential energy surface

As mentioned above, before deriving an analytical expression for the periodic PES $V(x, y, z)$, we tested commonly used functional forms for the He-surface interaction in analyzing He-atom scattering from metal and metal-oxide surfaces (see, e.g., Ref. 48).

1. The hard-corrugated-wall potential model

The hard-corrugated-wall (HWC) potential model is the simplest model using the eikonal approximation.[49] Very recently, it has been found to be a useful approximation in analyzing grazing scattering of atoms from the MgO(001) via the fast atom diffraction (FAD) technique.[48,50] The analytical expression of the helium-surface potential reads then as

$$V(x, y, z) = \begin{cases} 0 & \text{if} \quad z > \zeta(x, y) \\ \infty & \text{if} \quad z \leq \zeta(x, y) \end{cases}, \tag{1}$$

where $\zeta(x, y)$ is the so-called corrugation (or shape) function (CF). This function reflects the electronic density contours built up by the TiO_2(110) surface atoms.[51] The same model has been used to characterize the He−MgO interaction upon the analysis of diffraction patterns[52] via the He atom scattering (HAS) technique.[53] It is usually considered as an acceptable approximation if the incident energy of the incoming helium atom is of the same order of magnitude or larger than the well-depth of the He-surface potential. Since typical HAS measurements use atomic beams of thermal energy (10−100 meV) while the FAD method handles projectile energies up to some KeV and the calculated He−TiO_2(110) potential exhibits a well-depth of about 10 meV at the global minimum, the HWC approximation could be (in principle) considered as an acceptable zero-order approximation to rationalize both HAS and FAD data.

The corrugation function can be estimated from the effective corrugation function (ECF), $\zeta(x, y; \epsilon)$. This function depends on the incidence energy ϵ of the helium atom. It can be calculated from the classical turning points of the repulsive part of the He−TiO_2 potential satisfying the following implicit equation,

$$V(x,\ y; \zeta(x, y; \epsilon)) = \epsilon. \tag{2}$$

In order to determine the effective corrugation functions, we have selected nine ϵ values in the range [10–700] cm^{-1} and the ECFs have been determined by inverse interpolation with cubic splines. Figure 3 displays contour plots of the equipotential surfaces (ECFs) with $\epsilon = 50$ (left panel) and 500 cm^{-1} (right panel). The computed ECFs are found to be virtually indistinguishable from each other.

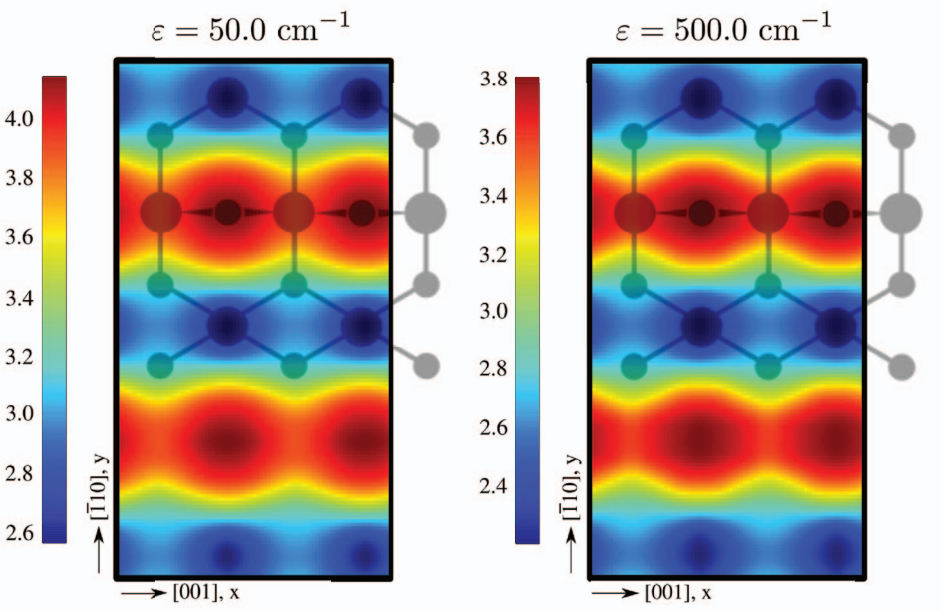

FIG. 3. Contour plots of the equipotential surfaces (effective corrugation functions) with energies $E = 50$ and 500 cm^{-1}. The reference geometry is located at the position of the Ti(5*f*) atom (center of the figure).

By accounting for the periodicity conditions, the effective corrugation functions can be expanded in a complex Fourier series as

$$\zeta(x, y; \epsilon) = \sum_{\mathbf{G}} \zeta_{\mathbf{G}}(\epsilon) e^{i\mathbf{G}\cdot\mathbf{R}}, \tag{3}$$

where the sum runs over all reciprocal two-dimensional lattice vectors defined as $\mathbf{G} = 2\pi(n/a_1, m/a_2)$, with a_1 and a_2 as the surface cell parameters (see above) and with $\mathbf{R} = (x, y)$ as a lattice vector defining a plane parallel to the surface. Hereafter the notation $\mathbf{G} = (n, m)$ will be used to index a reciprocal space vector for the sake of simplicity. Symmetry considerations allow to re-write Eq. (3) in a more compact form as

$$\zeta(x, y; \epsilon) = \sum_{(n,m)=(0,0)}^{(n_{max}, m_{max})} \zeta_{(n,m)}(\epsilon) \cos\left(\frac{2\pi n}{a_1} x\right) \cos\left(\frac{2\pi m}{a_2} y\right), \tag{4}$$

where the zero-order Fourier term $\zeta_{(0,0)}(\epsilon)$ represents the average of the z distances associated to the classical turning points of a He atom of energy ϵ (in the normal direction) scattering off the surface. This laterally averaged value decays monotonically as a function of ϵ (see the upper panel of Fig. S1, presented as supplementary material[41]). Following the model of Esbjerg and Nørskov,[51] the He-surface interaction energy is considered to be proportional to the local electron density at the He atom location. The decreasing behavior of the $\zeta_{(0,0)}(\epsilon)$ function with respect to ϵ thus reflects the deeper penetration of higher energy helium atoms into the surface electronic-density profile. On the other hand, the first-order Fourier terms $\zeta_{(1,0)}$ and $\zeta_{(1,0)}$ can be interpreted as the half of the corrugation amplitudes along the [001] and [$\bar{1}$10] directions, respectively. Higher-order terms ensure an accurate representation of the function.

The calculated effective corrugation functions were fitted to a discrete Fourier representation (Eq. (4)) by the nonlinear least square Levenberg-Marquart algorithm. Within the incidence energy range considered, the selection of $n_{max} = 2$ and $m_{max} = 3$ (i.e., a total of 12 Fourier terms) ensures maximum and mean square errors smaller than 0.01 and 0.03 Å, respectively. In fact, a very fast convergence rate with the number of $\mathbf{G}$ terms was obtained. In contrast to $\zeta_{(0,0)}(\epsilon)$, the $\mathbf{G} \neq \mathbf{0}$ terms vary very little as a function of the atomic beam incident energy (see the lower panel of Fig. S1, presented as supplementary material[41]). Hence, it is sensible to use an averaged corrugation function. The values of the $\zeta_{\mathbf{G}}$ matrix elements are also provided as supplementary material.[41] By averaging the effective corrugation functions over the considered range of incident energies, the calculated corrugation amplitudes along the main crystallographic directions are $\zeta_{(001)} = 0.090$ Å and $\zeta_{(\bar{1}10)} = 1.239$ Å. These values are of the same order of magnitude as the apparent corrugation measured through the scanning tunneling microscopy technique. For example, values of 0.14 (Ref. 54) and 1.2 Å (Ref. 55) have been reported for the corrugations in the [001] and [$\bar{1}$10] directions, respectively.

2. The corrugated-Morse potential model

The description of bound-state resonances observed in HAS measurements makes necessary the consideration of an attractive potential well within the model for the He-surface interaction. The CM potential model, originally proposed by Armand and Manson,[56] uses the following explicit form for the He-surface potential:

$$V(\mathbf{R}, z) = D\left\{\frac{1}{\nu_{\mathbf{0}}} e^{-2\alpha[z - z_e - \zeta(\mathbf{R})]} - 2e^{-\alpha(z - z_e)}\right\}, \tag{5}$$

where D is the well-depth, α is the stiffness parameter, and $\nu_{\mathbf{0}}$ is the average of the first term over the surface unit cell $\mathcal{A}$ of area S, $\nu_{\mathbf{0}} = \frac{1}{S}\int_{\mathcal{A}} e^{2\alpha\zeta(\mathbf{R})}\, d\mathbf{R}$. It is thus assumed that only the repulsive part of the potential is corrugated while the attractive part (second term) remains invariant under lateral displacements. This potential is assumed to support bound states agreeing with the experimentally determined absorption resonances.

By accounting for the $TiO_2(110)$-(1×1) surface periodicity and additional spatial symmetry properties of the system, the He-surface potential can be expanded in a real Fourier series as

$$V(\mathbf{R}, z) = \sum_{\mathbf{G}} V_{\mathbf{G}}(z) \cos(\mathbf{G}\cdot\mathbf{R}), \tag{6}$$

where the Fourier coefficients $V_{\mathbf{G}}(z)$ can be numerically calculated from

$$V_{\mathbf{G}}(z) = \frac{1}{S}\int_{\mathcal{A}} V(\mathbf{R}, z) \cos(\mathbf{G}\cdot\mathbf{R})\, d\mathbf{R}. \tag{7}$$

The Fourier coefficients of the interaction potential have a clear physical meaning, accounting for the coupling between the different diffraction channels. By inserting the analytical expression of $V(\mathbf{R}, z)$ from Eq. (5) into Eq. (6), explicit forms of the Fourier coefficients within the CM model are obtained

$$V_{\mathbf{G}}(z) = \begin{cases} D[e^{-2\alpha(z-z_e)} - 2e^{-\alpha(z-z_e)}] & \mathbf{G} = \mathbf{0}, \\ D\left(\frac{\nu_{\mathbf{G}}}{\nu_{\mathbf{0}}}\right) e^{-2\alpha(z-z_e)} & \mathbf{G} \neq \mathbf{0}, \end{cases} \tag{8}$$

where the terms $\nu_{\mathbf{G}}$ are defined as

$$\nu_{\mathbf{G}} = \frac{1}{S}\int_{\mathcal{A}} e^{2\alpha\zeta(\mathbf{R})} \cos(\mathbf{G}\cdot\mathbf{R})\, d\mathbf{R}. \tag{9}$$

Hence, within the CM potential model, non-diagonal Fourier coefficients $V_{\mathbf{G}\neq\mathbf{0}}(z)$ show a simple exponential form as a function of the vertical distance to the surface z while the $V_{\mathbf{G}=\mathbf{0}}(z)$ component has a one-dimensional Morse potential form. Typically, the non-diagonal Fourier coefficients are repulsive, increase rapidly as z decreases and their strengths decrease with $|\mathbf{G}|$.

For the sake of comparison, *numerical* Fourier coefficients $V_{\mathbf{G}}(z_k)$ have been obtained from Eq. (7) by first interpolating the calculated DFT energies on an equally spaced z-grid $\{z_k\}$ at a given lateral geometry (x, y). The numerical details can be found in the supplementary material.[41] The *numerical* coefficients are shown in Fig. 4. As clearly apparent from this figure, the *numerical* values $V_{(0,0)}$ (highlighted with black circles) fit very well with a Morse functional form

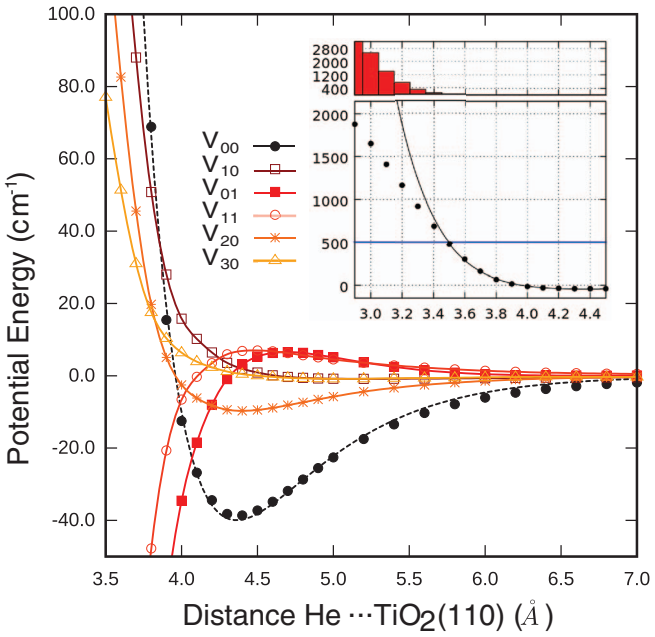

FIG. 4. Fourier coefficients of the interaction He−TiO_2(110)-(1×1) potential as a function of the vertical distance z from the surface (with $z = 0$ located at the surface Ti(5*f*) plane). The solid lines for non-diagonal coefficients $V_{\mathbf{G}} \neq \mathbf{0}$ are drawn with cubic splines. Inset panel: comparison between the V_{00} component obtained by fitting to a Morse potential (dashed line) and numerically (solid circles). The energy differences are shown in the upper (inset) panel.

(drawn with a black dashed line). Our fitting gives the values $D = 38.89 \pm 0.0021$ cm^{-1}, $\alpha = 1.675 \pm 0.017$ Å^{-1}, and $r_e = 4.3643 \pm 0.0044$ Å. As can be seen in the inset of Fig. 4, however, the fitted Morse potential energy curve departs from the *numerical* values at energies above 500 cm^{-1}. The *analytical* form of the corrugation function $\zeta(\mathbf{R})$ (see Sec. II A 1) can be inserted in Eq. (8) to get *analytical* expressions of the non-diagonal $V_{\mathbf{G}\neq\mathbf{0}}$ coefficients within the framework of the CM model. These coefficients are drawn along with the *numerical* values in the supplementary material (see Fig. S2 in Ref. 41). The *numerical* non-diagonal coefficients $V_{\mathbf{G}\neq\mathbf{0}}(z)$ depart noticeably from those obtained with the corrugated-Morse-potential model, specially the $\mathbf{G} = (n, m)$ components with n and/or m greater than 2. For example, as also apparent from Fig. 4, the *numerical* coefficient $V_{(0,3)}$ increases as z decreases whereas the opposite holds for the CM-based $V_{(0,3)}$ term (see Fig. S2 in Ref. 41). The CM-based Fourier series converges very rapidly so that the magnitude of the $V_{\mathbf{G}}$ coefficients with $|\mathbf{G}| > 3$ is very small. In contrast, the convergence rate of the *numerical* coefficients is extremely slow so that (in principle) a larger amount of diffraction channels would have to be included in a close-coupling calculation to get convergence. As pointed out by Wolken,[57] however, the number of diffraction channels to be included is not only determined by the structure of the potential coupling matrix but also and more directly by the corrugation amplitude, which is rather large in our case. On the other hand, the CM model is not able to account for the fine details of the *numerical* coefficients. The potential *anti-corrugation* is only qualitatively reflected in the *numerical* $V_{(0,1)}$ and $V_{(1,1)}$ coefficients (see Fig. 4), they increase as the helium atom approaches the surface, become equal to zero at $z = 4.32$ and 4.62 Å, respectively, and revert their signs closer to the surface. This feature, however, is lacking in the CM-based coefficients.

3. The three-dimensional Morse potential model

Finally, the DFT-PBE energies have been fitted to a three-dimensional Morse potential functional form

$$V(x, y, z) = D(x, y) \times \{e^{-\alpha(x,y)[z-z_e(x,y)]} - 2e^{-2\alpha(x,y)[z-z_e(x,y)]}\},$$

where all the Morse parameters are periodic functions with the symmetry of the underlying TiO_2(110)-(1×1) lattice. At variance with the CM potential model, this functional form accounts for the lateral modulation of the equilibrium distance z_e and the well-depth D_e induced by the strong structural corrugation of the TiO_2(110) surface. The detailed fitting procedure is provided in the supplementary material.[41] Briefly, the DFT-PBE energies obtained at a given lateral position (x, y) are fitted to a z-dependence Morse potential. The continuity of the He-surface potential interaction along the z variable for each (x, y) is obviously ensured, but not the reciprocal. The functions $D(x, y)$, $\alpha(x, y)$, and $z_e(x, y)$ functions are shown in the left-hand panels of Fig. 5. It can be seen that these functions may not be smooth enough. For example, the function $\alpha(x, y)$ displays two shoulders at the neighborhoods of the bridging oxygen atoms while the function $D(x, y)$ has a small roughness around the Ti(5*f*) site. These small oscillations arise from the imprecision of the electronic structure calculation itself and are therefore a numerical artifact that could affect further dynamical calculations. As described in the supplementary material,[41] these functions were further Fourier expanded so that an analytical functional for the final He-surface PES was obtained

$$P(x, y) = \sum_{n=0}^{2}\sum_{m=0}^{3} P_{\mathbf{G}} \cos\left(\frac{2\pi n}{a_1}x\right) \cos\left(\frac{2\pi m}{a_2}y\right)$$

with $P \equiv D, \alpha, z_e$. As clearly apparent in the right-hand panels of Fig. 5, this procedure gives functional Morse parameters exhibiting smooth and completely regular profiles.

The robustness of the 3DM functional form was also tested by calculating the Fourier coefficients of the potential as a function of z, having an analytical expression within this model. As can be seen in Fig. S3 from Ref. 41, the 3DM Fourier coefficients keeps the same sign as the *numerical* Fourier coefficients along the z variable. This is in contrast with the CM potential model which inverts the sign of some Fourier coefficients. Also at variance with the CM coefficients, the special profile of the $V_{(0,1)}$ and $V_{(1,1)}$ terms, reflecting somehow the potential *anti-corrugation*, is preserved through the fitting to the 3DM potential model. On the other hand, the 3DM functional form attains an important advantage over the *numerical* representation: the strength of the Fourier coefficients decreases rapidly with $|\mathbf{G}|$. For example, the value of the $V_{(3,3)}$ term is already negligible.

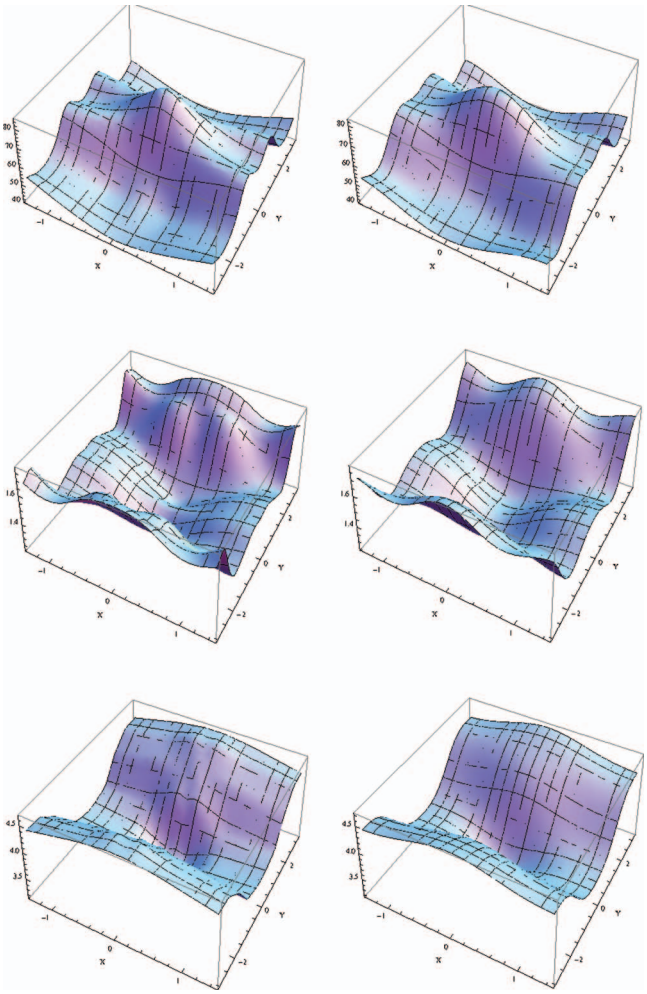

FIG. 5. Fittings of the Morse potential parameters $D(x, y)$ (upper panels), $\alpha(x, y)$ (center panels), and $r_e(x, y)$ (lower panels). Left-hand panels: parameters obtained after fitting to a Morse potential of the DFT energies at each lateral location (x, y). Right-hand panels: "analytical" parameters which have been calculated by applying least-square minimization to the calculation of the Fourier expansion coefficients.

B. On the long-range dispersive interaction and the pairwise approximation

As mentioned in the Introduction, local and semi-local DFT functionals such as PBE neglect long-range dispersive interaction contribution. By using both Grimme's scheme (e.g., the so-called DFT-D2 (Ref. 58)), in which damped $-C_6/R_6$ corrections are included, and the first principles van der Waals density functional (termed vdW-DF) approach[38] incorporating non-local correlation, the long-range dispersive interaction can be accounted for in DFT calculations. The PBE-D2 approach was previously tested for the He−TiO_2 interaction by using a small model cluster of stoichiometry $(TiO_2)(H_2O)_3$ in Ref. 27. The PBE-D2 binding energy overestimated the energy obtained at CCSD level by a factor of ∼3.5. A similar factor (∼4) is found by comparing the energies obtained at PBE and PBE-D2 levels, using the periodic approach presented here. Some preliminary calculations using the original formulation of the vdW-DF approach[38] (i.e., using the revPBE (Ref. 59) functional for the exchange energy) are presented as supplementary material.[41] These additional revPBE-vdW calculations were carried out by using the projector-augmented wave method implemented in the VASP code.[60,61] Specifically, the revPBE-vdW interaction potential as a function of the vertical height z above the Ti(5*f*) site was calculated and compared with that obtained either at the LMP2 level on a model cluster of stoichiometry $(TiO_2)_9(H_2O)_{16}$,[27] or using the periodic PBE approach. The revPBE-vdW well-depth differs by less than 15% from PBE and LMP2 values, while the revPBE-vdW (PBE) equilibrium distance is about 0.15 Å larger (shorter) than its LMP2 counterpart. The overestimation (underestimation) of the adsorbate-surface distance (the binding energy) by revPBE-vdW is in line with a recent analysis on the application of vdW-DFs to solids[62] (to H-bonded duplexes[63]).

Even better potentials could probably be obtained by following the procedure of Michaelides and co-workers to design modified vdW-DFs as in Ref. 62. Concerning DFT-D flavors, DFs "mimicking" closely the short-range Hartree-Fock repulsive behaviour, such as revPBE, have been found to perform better in DF+D constructions than pure PBE on weakly hydrogen-bound systems (see, e.g., Refs. 32 and 64). Another idea that has been put forward by Pernal *et al.*[65] consists in using dispersionless DFs on top of which "+D" corrections can be surely added. As mentioned in the Introduction, localized molecular orbital energy decompositions and SAPT calculations, such as those carried out by Jordan and co-workers,[37] using a small cluster as a model system of the He−TiO_2 interaction (see above), can also be useful. Work in these directions is currently in progress.

In this work, the laterally averaged potential (LAP), $V_{\mathbf{G}=\mathbf{0}}(z)$, was slightly modified to account for the correct $-1/z^3$ scaling by adding the term $-f(z; z_0, a)(\frac{C_3}{z^3})$, where the expression of the damping function reads

$$f(z; z_0, a) = \frac{1}{2}\left\{1 + \tanh\left[\frac{z - z_0}{a}\right]\right\}. \qquad (10)$$

It should be noted than the same LAP is obtained from the CM and the 3DM models. The correction would start affecting the LAP from approximately $z \geq z_0 - 2a$. The values of the z_0 and a parameters were fixed to 6.0 and 0.5 Å, respectively. They were selected so that the minimum region of the potential is kept almost unaltered and the continuity of the functions $V_{\mathbf{G}=\mathbf{0}}(z)$, $V'_{\mathbf{G}=\mathbf{0}}(z)$ (first-derivative), and $V''_{\mathbf{G}=\mathbf{0}}(z)$ (second derivative) is ensured. As mentioned in the Introduction, the pragmatic justification for the former condition is that the model cluster LMP2 calculations provided a shaft region agreeing very well with that obtained with the periodic DFT-PBE approach.

Concerning the C_3 prefactor, we adopted the approach described by Johnson and Hinde in Ref. 66 where it was applied to the He−MgO(100) interaction to obtain an effective C_3 coefficient. Within this framework, the He−TiO_2(110) interaction is modeled as a sum of pairwise additive He−Ti and He−O attractive interactions with a Lennard-Jones $-C_{6,X}/R^6$ form, with X = Ti or O, allowing to get an analytical expression of the C_3 coefficient as a function of the $C_{6,X}$ terms. By using the Slater-Kirkwood formula, these terms are expressed as a function of the static polarizabilities for He (Ref. 67) and for the Ti^{4+} and O^{2-} ions in TiO_2,[68] and

the effective number of valence electrons.[67] We obtained the values $C_{6,\mathrm{Ti}} = 1.798$ a.u. and $C_{6,\mathrm{O}} = 11.470$ a.u, and an effective He−TiO_2(110) coefficient (referred to as C_3^{LJ}) of 245.809 meV Å^3. It is stressed that a similar value is obtained with the $C_{6,X}$ coefficients within the DFT-D2 ansatz of Grimme[58] (241.794 meV Å^3). These values are almost a factor of six larger than the prefactor obtained from fitting the DFT-PBE results above ($C_3^{\mathrm{fit}} = 38.988$ meV Å^3). This prefactor C_3^{fit} remained practically unaltered with the lateral position (x, y). As mentioned in Refs. 66 and 67, the actual value is expected to be smaller than the prefactor C_3^{LJ} because of surface dielectric screening effects in successively deeper layers. Since DFT-PBE neglects long-range correlation (i.e., C_3^{fit} is just an adjustable parameter), it can be expected that the actual value might lie between the values of C_3^{fit} and C_3^{LJ}. The number and energies of the bound states supported by the LAP potential are very sensitive to the value of the prefactor. These are presented as supplementary material.[41] Therefore, direct experimental information on selective absorption resonances, as already reported for the He−MgO(001) case,[69] would be very useful in assessing the reliability of the corrected LAP. In order to assess the role of the long-range dispersive term, dynamics calculations were carried out by using both the pure LAP and the corrected LAP with the damped $-C_3^{\mathrm{LJ}}/z^3$ term (referred to as LAP+C_3^{LJ}).

Before closing this section, we would also like to mention that the adequacy of the pairwise additive approximation was tested on the He_2−TiO_2(110)-(1×1) case. The results are presented as supplementary material.[41] Briefly outlined, relative errors within the effective range of interatomic He−He distances in liquid helium are found to be lower than 8%. However, the quantitative accuracy deteriorates rapidly beyond this regime.

III. COLLISION OF A HELIUM DROPLET WITH THE TiO_2(110)-(1×1) SURFACE

The dynamical evolution of a helium nanodrop on the surface was followed by performing TDDFT calculations.[20] This is a general algorithm for solving a three-dimensional time-dependent Schrödinger-like equation for the effective helium wave-function. This TDDFT method relies on a DFT approach differing largely from the DFT-PBE approach applied to the electronic structure problem. While the latter is used within the Kohn-Sham formulation of DFT (Ref. 55), the former is an orbital-free method in which the kinetic energy is calculated by a functional of the density alone. Also, the density functional applied to the helium motion was designed to reproduce bulk experimental properties of liquid ^{4}He (Ref. 70) while the PBE functional[43] was constructed to satisfy different physical constraints as having the correct free-electron gas limit. The details of the TDDFT approach has been provided elsewhere (see, e.g., Ref. 20) so that only a brief outline is provided here.

A. Outline of the method and computational setup

Within the DF approach, the energy of a helium nanodrop composed by 300 ^{4}He atoms at zero temperature is first written as a function of the effective helium wave-function $\Psi(\mathbf{r}) = \sqrt{\rho(\mathbf{r})}$:

$$E[\Psi] = \frac{\hbar^2}{2m_{\mathrm{He}}}\int d\mathbf{r}\,|\nabla\Psi|^2 + \int d\mathbf{r}\,\mathcal{E}_{\mathrm{He-He}}[\rho] + \int d\mathbf{r}\,\rho(\mathbf{r})V_{\mathrm{ext}}^{\mathrm{He-TiO_2}}(\mathbf{r}),$$

where the $\mathcal{E}_{\mathrm{He-He}}[\rho]$ term denotes the helium-helium potential energy density accounting for mean-field and short-range correlation effects, and $V_{\mathrm{ext}}^{\mathrm{He-TiO_2}}(\mathbf{r})$ represents the external He-TiO_2 potential acting on the helium drop. For this work we have chosen the finite-range Orsay-Trento density functional.[70] This functional is designed omitting the term mimicking the black-flow effects (i.e., elementary excitations within superfluid ^{4}He). Previous studies[71] have shown that the incorporation of this term have minor effects in the dynamical evolution and a high computational cost. The explicit functional form of $\mathcal{E}_{\mathrm{He-He}}[\rho]$ is given in Ref. 70, and can be written (in abbreviated form) as

$$\mathcal{E}_{\mathrm{He-He}}[\rho] = \frac{1}{2}\int d\mathbf{r}\int d\mathbf{r}'\rho(\mathbf{r})\rho(\mathbf{r}')\,V_{\mathrm{He-He}}(|\mathbf{r}-\mathbf{r}'|) + \int d\mathbf{r}\,\mathcal{E}_c(\mathbf{r}) + \int d\mathbf{r}\,\frac{\rho(\mathbf{r})}{2}m_{\mathrm{He}}|\mathbf{v}(\mathbf{r})|^2,$$

where $V_{\mathrm{He-He}}$ is the He−He interaction potential screened at short distances. The last two terms account for short-range correlation effects arising from the hard-core of the He−He potential, and the hydrodynamic current, respectively. By minimizing $E[\Psi]$ with respect to variations of the effective wave-function $\Psi(\mathbf{r})$ one obtains the ground-state wave-function $\Psi_0(\mathbf{r})$, fulfilling

$$-\frac{\hbar^2}{2m_{\mathrm{He}}}\Delta\Psi_0 + \left\{\frac{\partial\mathcal{E}_{\mathrm{He-He}}[\rho]}{\partial\rho} + V_{\mathrm{ext}}^{\mathrm{He-TiO_2}}\right\}\Psi_0 = \mu\Psi_0, \tag{11}$$

where μ is the helium chemical potential that ensures the conservation of the number of helium atoms. On the other hand, the dynamical evolution of the helium nanodrop evolves according to the time-dependent equation,

$$\frac{\partial\Psi(\mathbf{r},t)}{\partial t} = -\frac{\imath}{\hbar}\times\left\{-\frac{\hbar^2}{2m_{\mathrm{He}}}\Delta + \frac{\partial\mathcal{E}_{\mathrm{He-He}}[\rho]}{\partial\rho} + V_{\mathrm{ext}}^{\mathrm{He-TiO_2}}(\mathbf{r})\right\} \times\Psi(\mathbf{r},t). \tag{12}$$

The differential operators are discretized using 13-point finite-difference formula (although 25-point formula was seldom employed to test the quality of the solution). The time-dependent Schrödinger-type equation is solved numerically with Hamming's method of order five[72] while a fourth order Runge-Kutta scheme is used for the first four iterations. Unitarity of the evolution is ensured by using a time step Δt of 2×10^{-4} ps. We work in three-dimensional Cartesian coordinates that allow to exploit fast Fourier transformation techniques[73,74] in the calculation of the convolution integrals entering the definition of the effective He−He potential.[70] The simulation is performed using 256 × 256 × 128 grid for the FFT. The integration steps have been selected so that the dimension of the 3D box is 200 × 200 × 60 Å^3 ($\Delta x = \Delta y = 0.781$ Å, $\Delta z = 0.469$ Å). These values are chosen so that

one has a large enough space in the xy −plane for the drop to expand through the surface. We chose a dense z mesh which is capable of accommodating the short-wavelength density oscillations associated with high-momentum components of the incoming droplet.

The wave-function is damped upon reaching the box boundaries to avoid its artificial reflection. We employed the damping procedure described in Ref. 20 but with the damping-free region as a cylinder plus a plane parallel to the surface instead of a sphere. In practice, the time-dependent Schrödinger-type equation governing the evolution of the wave-packet is modified as

$$\frac{\partial \Psi(\mathbf{r},t)}{\partial t} = \frac{(\imath + \Lambda(\mathbf{r}))}{\hbar}\left\{-\frac{\hbar^2}{2m_{\mathrm{He}}}\Delta + \frac{\partial \mathcal{E}_{\mathrm{He-He}}[\rho]}{\partial \rho}\right\}\Psi(\mathbf{r},t) - \frac{\imath}{\hbar}\left\{V_{\mathrm{ext}}^{\mathrm{He-TiO_2}}(\mathbf{r})\right\}\Psi(\mathbf{r},t),$$

where the damping function $\Lambda(\mathbf{r})$ can be expressed in cylindrical coordinates ($\rho = \sqrt{x^2+y^2}$ and z) as

$$\Lambda(\rho,z) = \sum_{s=\rho,z}\Lambda_0\left[1+\tanh\left(\frac{s-s_0}{a}\right)\right], \qquad (13)$$

where $z = 0$ is the position of the TiO_2 surface, $x = y = 0$ being the line connecting it with the helium droplet center of mass. The dimensionless parameter Λ_0 is fixed to 2.5, and the values of ρ_0, z_0, and a are set to 90, 57.4, and 5 Å, respectively. The wave-packet is thus absorption-free in a cylinder of radius $\rho < \rho_0 - 2a$ and height $z < z_0 - 2a$.

We have used the laterally averaged He−TiO_2(110)-(1×1) potential, depending only on the z height above the surface $V_{\mathrm{ext}}^{\mathrm{He-TiO_2}}(z)$, with and without the damped $-C_3^{\mathrm{LJ}}/z^3$ term (see Sec. II). This is the most sensible choice compatible with the hydrodynamical description of He and the phenomenological treatment of the He−He correlations in the functional. The short-range correlations are taken into account in by means of the coarse-grained density, an averaged density over a sphere of radius $h = 2.19$ Å. In this procedure one is assuming that the energy functional does not depend on the details of the structure at lengths scales smaller than h, as this structure will be smoothed out by correlations. The surface corrugation was taking into account, however, in classical dynamics calculations by using the 3DM potential model (see Sec. III C).

B. Evolution of the helium density profiles

The initial helium wave-function can be written as

$$\Psi(\mathbf{r}, t=0) = \Psi_0(\mathbf{r})e^{\imath \mathbf{k}_0\cdot\mathbf{r}}, \qquad (14)$$

with $\rho_0(\mathbf{r})$ as the helium density obtained by minimizing the energy without the adsorbing He−TiO_2 potential (Eq. (11) without the term $V_{\mathrm{ext}}^{\mathrm{He-TiO_2}}$). We have added a boost $\mathbf{k}_0 = -1.26\,\hat{e}_z$ Å^{-1} in order to provide the helium nanodrop with a collective initial velocity towards the surface plane of 200 m/s, according with the experimental setup.[7] The dynamical simulation starts by placing the helium droplet mass center at 27.4 Å from the surface.

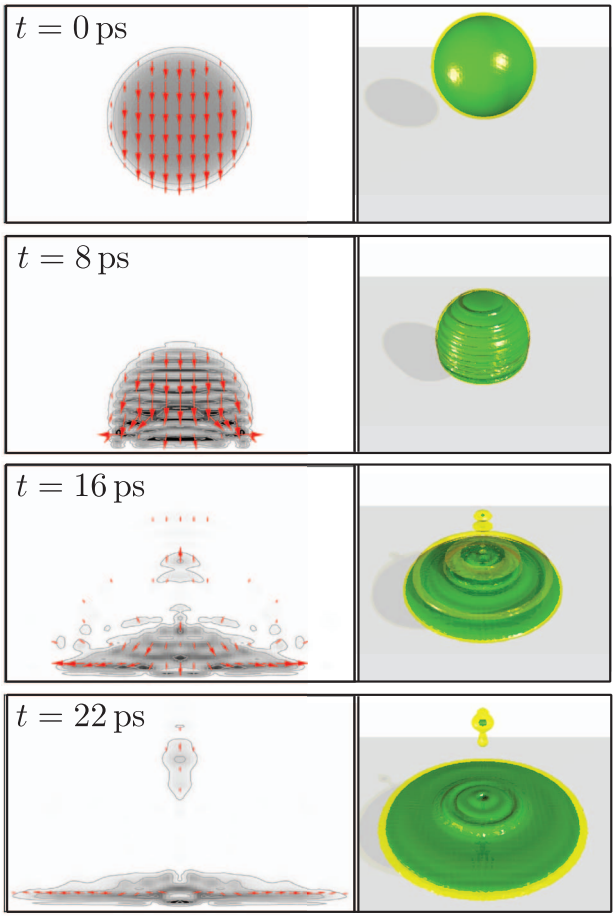

FIG. 6. Snapshots showing the dynamical evolution of the helium density profiles associated to a $^4He_{300}$ drop at impact with the TiO_2(110)-(1×1) surface. The display frames are 80 × 50 Å^2. The TiO_2(110) surface is located at 2.4 Å from the bottom edge of the box. Left-hand panel: 2D contours of the helium density profiles. Red arrows indicate the current field with a size proportional to the current intensity at a local point. The panels correspond to times $t = 0$, 8, 16, and 22 ps. The clearer the color, the higher the helium density. Right-hand panel: iso-probability helium density surfaces. See also the TDDFT movie presented as supplementary material.[41]

Figure 6 shows the evolution of the helium density profile of the ^{4}He droplet during the first 22 ps. The spreading of the helium droplet at impact can be followed from the sequence of snapshots in this figure. The distortion of the drop due to the interaction with the TiO_2 surface is already apparent at $t = 8$ ps, when a pressure density wave starts to propagate due to the compression of the helium drop. A feature worth mentioning is that although the pressure density wave is propagating backwards from the surface along the symmetry axis z, the direction of the local current field (indicated by arrows in the left-hand panels of Fig. 6) is almost always pointing towards the surface. The density waves that are travelling up through the droplet, while the current field is going down are associated to phononic excitations of the helium droplet. The spreading starts at about 10 ps, with the mean square radius of the droplet growing linearly in time.[41] At about $t = 16$ ps, fractions of the total density are expelled backwards from the helium droplet. Then at $t = 22$ ps, the drop continues expanding along the (x, y) plane. The simulation was necessarily finished when the droplet reached the edges of the

simulation box. The value of the sticking probability converged to 0.7 and the velocity in the spreading was estimated to be 137.8 m/s (see Sec. S7 in the supplementary material[41]). Therefore, the droplet losses about 90 particles due to the impact with the surface. We also stress that minor differences were observed when the $-C_3^{LJ}/z^3$ long-range term was included[41] so that the calculated velocity of spreading was the same within numerical accuracy.

Let us now compare our results with those obtained by considering weakly attractive surfaces.[1] In contrast with weak adsorbers such as the Cs surface[1] (it is not wet by ^{4}He at very low temperatures), our TDDFT results show that the rutile surface is a rather strong adsorber. Not only ^{4}He wets the surface at $T = 0$ but also density peaks with $\rho = 0.08$ Å^{-3} (i.e, a value which is close to the helium solidification point[75]) are found for the equilibrium configuration of a helium slab deposited on top of the surface. However, some similarities were found with the equilibrium density profiles reported for the Cs surface in Ref. 1 such as the formation of a thin precursor layer separated by a quasi-node from the layer with the highest density, and a quasi-linear scaling dependence of the mean square radius of the droplet as a function of time in the earlier stage of the spreading process. The velocity of spreading is, however, much larger in our case (138 vs. 50 m/s from Ref. 1) due to both the stronger attraction exerted by the TiO_2(110) surface and the high velocity of the incoming droplet.

Finally, it should be stressed that the spreading process, which is characterized by a plastic deformation of the incoming species,[17] differs from the soft-landing case, in which collision induced deformations are elastic.[17] However, it is also worth-mentioning that the spreading of the helium droplet upon impact is consistent with the "intact" soft-landing deposition of an embedded species. The discussion on how the helium carrier spreading affects the deposition of a catalytic species, formed inside the droplet, has been left for a forthcoming paper. It is also recalled that the chosen Orsay-Trento density functional describes helium properties at $T = 0$. Therefore, a zero temperature of both the helium droplet and the surface is assumed. In the experimental setup,[6] the produced helium droplets cools very rapidly, reaching a temperature (0.37 K) below the superfluid transition temperature (2.17 K). On the other hand, substrate samples at room temperature (about 300 K) are employed.[7] Finite-temperature (phonon-mediated) surface effects are not expected to affect the dynamical process described here too much because these effects typically develop on the time scale of nanoseconds (i.e., much longer that the spreading process). However, these effects would ultimately lead to the helium droplet evaporation during the thermalization process with the surface.

C. TDDFT vs. classical dynamics

For the sake of comparison, we also performed classical trajectory (CT) calculations. The analytical He−He potential derived by Aziz and Slaman[76] was employed to account for the He−He interaction. A recent study using full-configuration-interaction (FCI) calculations with increasing basis set sizes on the helium dimer[27] showed the convergence trend of FCI results (i.e., energy and wave-function of the bound state) to those obtained with the Aziz-Slaman potential. Concerning the He−TiO_2 interaction, we used the LAP, the LAP with the damped $-C_3^{LJ}/z^3$ term (referred to as LAP+C_3^{LJ}), and the 3DM potential models.

The density of the isolated $^4He_{300}$ cluster obtained with the DFT approach at $T = 0$ was sampled by using the random walk Metropolis algorithm. To avoid the cluster disintegration, we imposed a minimal distance of 3 Å between each helium atom pair. Newton's equations of motion were solved through numeric integration by using the velocity Verlet algorithm[77] with a time step of 0.005 ps. In this way, the conservation of energy was better than 1 in 10^7. Alternative methods for classical dynamics propagations as Beeman's algorithm were proved, providing an almost identical picture. The chosen Verlet algorithm was found to be faster in our case.

The CT calculation started by assigning zero initial velocities to the helium atoms within the cluster. Next, a thermalization run of 20 ps at 0.1 K was carried out by using the Berendsen thermostat[78] with a time step of 0.04 ps.[78] This was followed by a simulation run of 600 ps without temperature control to ensure that the cluster is stable. The cluster center-of-mass was then placed at 25 Å from the TiO_2(110) surface and the helium atoms were provided with an initial velocity directed perpendicular to the surface, corresponding to the droplet collective velocity of 200 m/s in the experiment.[7] With this setup, we obtained the snapshots displayed in Fig. 7. They correspond to one classical trajectory from the 88 trajectories considered[41] and the LAP model.

All our CT calculations show the helium droplet evaporation after the collision, with a sticking probability below 3%. By comparing the results obtained with the LAP and the LAP+C_3^{LJ} models (see Figs. S8 and S9 in Ref. 41), the minor influence of the long-range correction is apparent so that the lateral (z-dependent) distributions are practically coincident. On the other hand, when the corrugation of the potential is considered through the 3DM model, the droplet evaporation process becomes faster. At $t = 20$ ps (i.e., after the impact), the fraction of evaporated He atoms is about 10% larger in the 3DM case. This minor difference could be rationalized by the presence of more steeply repulsive potential regions (i.e., where the protruding oxygen atoms are located) when the droplet is expanded along the (xy) plane (see also the snapshot at $t = 16$ ps in Fig. 7). The fraction of evaporated He atoms scales as $1/t^3$ and its asymptotic value is above 0.97, whatever the potential model be. Overall, our CT calculations indicate that the collision dynamics is mainly governed by the repulsive part of the He−TiO_2 PES.

Let us see how these results compare with those obtained with the TDDFT method. As can be seen by contrasting Figs. 6 and 7, the snapshots reveal a similar global picture up to $t = 16$ ps: the compression (extension) of the cluster along the symmetry z axis (xy plane) arising from the attraction with the TiO_2(110) surface. At very close distances to the surface, however, the picture changes very significantly (snapshots at $t = 22$ ps): while the TDDFT method discloses the spreading of the helium droplet, forming a thin film above the substrate with a relatively low fraction (∼30%) expelled backwards,

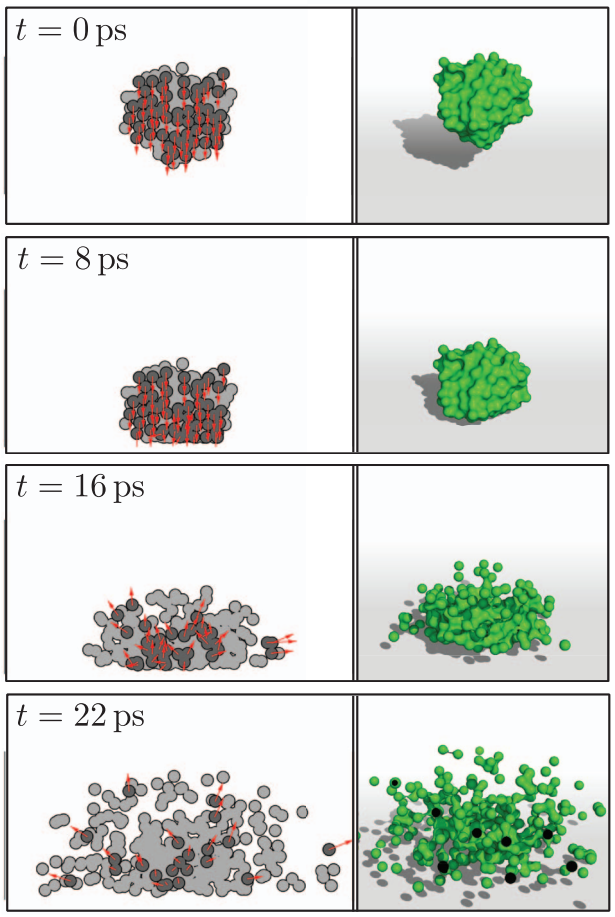

FIG. 7. Snapshots showing the classical dynamics evolution of a $^4He_{300}$ cluster at impact with the $TiO_2(110)$-(1×1) surface. The $TiO_2(110)$ surface is located at 25 Å from the helium cluster center-of-mass where the origin of the reference system is located. The panels correspond to times $t = 0$, 8, 16, and 22 ps. Red arrows indicate the velocity vector of the helium atoms with $-1.5 < z < 1.5$ Å (those marked with dark-gray colored spheres). The spherical helium atom surfaces with van der Waals radii were added to facilitate the visualization. See also the MD movie presented as supplementary material.[41]

CT calculations predict the splashing of the droplet and evaporation of the helium atoms at impact. Once again, this result highlights that the collision process, at the high velocity of the droplet in the experimental measurements, is very sensitive to the repulsive region of the He−TiO_2 interaction: the short-range He−He correlations, which are phenomenologically accounted for within the TDDFT method, play a crucial role in keeping the helium atoms together during the impact with the substrate (i.e., "surviving" to the repulsive part of the He-surface interaction). As mentioned above, our dynamics calculations have been accomplished assuming a (rigid) surface at $T = 0$. Molecular dynamics simulations considering a thermal vibrating surface could result in a larger degree of spreading of the helium droplet than that obtained from our CT calculations.

IV. SUMMARY AND CONCLUDING REMARKS

As a first step towards a microscopic description of helium droplet mediated deposition of catalytic species on surfaces, we studied the collision of a helium droplet with the $TiO_2(110)$-(1×1) surface where the He-surface interaction was computed from first principles. Based on a previous study,[27] we adopted a periodic DFT-PBE approach to perform the electronic structure calculations on a three-dimensional grid. Consistently, a time-dependent DFT approach, which was previously developed and proved to study different dynamical process in helium droplets,[20] has been chosen to describe the helium nuclear motion.

The first part of this work has been devoted to providing and analyzing analytical functional forms for the He−$TiO_2(110)$-(1×1) PES by fitting the calculated DFT-PBE interaction energies. Being aware of the necessity (and lacking) of this analytical PES both to carry out model calculations of helium atom diffraction and to interpret the corresponding experimental patterns, we analyzed two model He-surface potentials used in this context: the HCW and the CM potential models. Whereas the results obtained with the HCW potential model are useful in providing the structural corrugation of the surface, no information on selective-adsorption resonances can be obtained. On the other hand, the well region of the laterally averaged He-surface and supported bound states is properly described within the CM potential model, but it is unable to provide fine details of the potential as the evidenced *anti-corrugation* and its change of sign to corrugation at close He-surface distances. Moreover, the third-order potential Fourier coefficients are found to invert the signs of those numerically calculated from the DFT-PBE energies. Finally, we propose a 3DM potential model for several reasons. First, it is able to reproduce the potential *anti-corrugation*. Second, the imprecision of the electronic structure calculations is smoothed out. Third, the convergence rate of the Fourier series coefficients to zero as $|\mathbf{G}|$ increases is faster. The laterally averaged potential was further corrected by adding a damped $-C_3/z^3$ term. Next, the additive pairwise model for the He_N-$TiO_2(110)$ potential was proved for $N = 2$, demonstrating its accuracy as long as the interatomic He−He distances are within the effective range in liquid helium.

The second part of this paper has been focused on the outcome of TDDFT calculations for the evolution of a $^4He_{300}$ cluster upon collision with the $TiO_2(110)$ surface at $T = 0$. Our TDDFT results predict a fast spreading (a few tens of picoseconds) of the helium droplet on the substrate, with the sticking probability at ∼70%. In contrast, classical dynamics results show the splashing of the helium cluster at impact, with the trapping probability below 0.03 irrespective of the potential model considered. Additional correction of the potential with a $-C_3/z^3$ long-range tail is proved to attain a minor influence on the dynamics: due to the high velocity of the helium droplet (200 m/s from Ref. 7) the collision process is mainly driven by the repulsive part of the He−$TiO_2(110)$ PES. Therefore, short-range correlation effects, which are accounted for in the TDDFT formulation, play a key role in keeping the helium atoms together during the impact. Altogether, our dynamics calculations therefore highlight the importance of using a quantum-mechanical formulation to characterize accurately the dynamical evolution of the helium density in the collision with a prototype metal-oxide surface at $T = 0$. This work thus provides the basis for a further

theoretical study of helium mediated deposition of catalytic species, which has been monitored experimentally.[7] This issue will be addressed in the second paper of this series.

ACKNOWLEDGMENTS

We warmly thank Manuel Barranco and Pablo Villarreal for stimulating discussions and very useful suggestions. We also would like to thank Andrey Vilesov for useful exchanges. This work has been performed under Grant Nos. FIS2011-29596-C02-01 and FIS2011-28617-C02-01 from DGI, Spain (FEDER), Grant No. 2009SGR1289 from Generalitat de Catalunya, and Grant No. CCG08-CSIC/ESP-3680 from CSIC-CM. The support of COST Action CM1002 (CODECS) and the MICINN Grants Nos. FIS2007-62006 and FIS2010-18132 are also gratefully acknowledged. N.F.A. has been supported by a predoctoral JAE fellowship from the CSIC and D.M. by the ME (Spain) FPU program, Grant No. AP2008-04343. The calculations were performed at the Cesga Super-Computer Center (Galicia) and the Computer Centers at the IFF (CSIC) and the Centro Técnico de Informática (CTI, CSIC).

[1]L. Giagomazzi, F. Toigo, and F. Ancilotto, Phys. Rev. B **67**, 104501 (2003).
[2]M. Bosinsegni, Phys. Rev. B **70**, 193411 (2004).
[3]J. Turnbull and M. Bosinsegni, Phys. Rev. B **76**, 104524 (2007).
[4]F. Ancilotto, M. Barranco, E. S. Hernández, and M. Pi, J. Low Temp. Phys. **157**, 174 (2009).
[5]J. P. Toennies and A. F. Vilesov, Angew. Chem., Int. Ed. **43**, 2622 (2004).
[6]V. Mozhayskiy, M. N. Slipchenko, V. K. Adamchuk, and A. F. Vilesov, J. Chem. Phys. **127**, 094701 (2007).
[7]E. Loginov, L. F. Gómez, and A. F. Vilesov, J. Phys. Chem. A **115**, 7199 (2011).
[8]G. E. Johnson, Q. Hu, and J. Laskin, Annu. Rev. Anal. Chem. **4**, 83 (2011).
[9]V. Franchetti, B. H. Solka, W. E. Baitinger, J. W. Amy, and R. G. Cooks, Int. J. Mass Spectrom. Ion Phys. **23**, 29 (1977).
[10]S. A. Miller, H. Luo, S. J. Pachuta, and R. G. Cooks, Science **275**, 1447 (1997).
[11]T. A. Blake, Z. Ouyang, J. M. Wiseman, Z. Takáts, A. J. Guymon, S. Kothari, and R. G. Cooks, Anal. Chem. **76**, 6293 (2004).
[12]X. Tong, L. Benz, P. Kemper, H. Metiu, M. T. Bowers, and S. K. Buratto, J. Am. Chem. Soc. **127**, 13516 (2005).
[13]L. Benz, X. Tong, P. Kemper, Y. Lilach, A. Kolmakov, H. Metiu, M. T. Bowers, and S. K. Buratto, J. Chem. Phys. **122**, 081102 (2005).
[14]W. E. Kaden, T. Wu, W. A. Kunkel, and S. L. Anderson, Science **326**, 826 (2009).
[15]S. N. Rashkeev, S. Dai, and S. H. Overbury, J. Phys. Chem. C **114**, 2996 (2010).
[16]X. Tong, L. Benz, P. Kemper, H. Metiu, M. T. Bowers, and S. K. Buratto, J. Am. Chem. Soc. **127**, 13516 (2005).
[17]W. Harbich, in *Metal Clusters at Surfaces, Clusters Physics*, edited by K. H. Meiwe-Broer (Springer, Berlin, 2000).
[18]M. Moseler, H. Häkkinen, and U. Landman, Phys. Rev. Lett. **89**, 176103 (2002).
[19]A. Hernando, M. Barranco, M. Pi, E. Loginov, M. Langlet, and M. Drabbels, Phys. Chem. Chem. Phys. **14**, 3996 (2012).
[20]D. Mateo, D. Jin, M. Barranco, and M. Pi, J. Chem. Phys. **134**, 044507 (2011).
[21]U. Diebold, Surf. Sci. Rep. **48**, 53 (2003).
[22]T. L. Thomson and J. T. Yates, Jr., Chem. Rev. **106**, 4428 (2006).
[23]M. Grätzel, Nature (London) **414**, 338 (2001).
[24]M. Haruta, Catal. Today **36**, 153 (1997).
[25]A. S. Mazheika, T. Bredow, V. E. Matulis, and O. A. Ivashkevich, J. Phys. Chem. C **115**, 17368 (2011).
[26]A. J. C. Varandas, J. Phys. Chem. A **114**, 8505 (2010).
[27]M. P. de Lara-Castells, N. F. Aguirre, and A. O. Mitrushchenkov, "Physisorption of helium on a TiO2(110) surface: Periodic and finite cluster approaches," Chem. Phys. (in press).
[28]M. P. de Lara-Castells and A. O. Mitrushchenkov, J. Phys. Chem. C **115**, 17540 (2011).
[29]U. Birkenheuer, P. Fulde, and H. Stoll, Theor. Chem. Acc. **116**, 398 (2006).
[30]C. Pisani, M. Busso, G. Capecchi, S. Casassa, R. Dovesi, L. Maschio, C. Zicovich-Wilson, and M. Schütz, J. Chem. Phys. **122**, 094113 (2005).
[31]R. Martínez-Casado, G. Mallia, D. Usvyat, L. Maschio, S. Casassa, M. Schütz, and N. M. Harrison, J. Chem. Phys. **134**, 014706 (2011).
[32]S. Grimme, Comput. Mol. Sci. **1**, 211 (2011).
[33]A. J. Cohen, P. Mori-Sánchez, and W. Yang, Chem. Rev. **112**, 289 (2012).
[34]A. Michaelides, Appl. Phys. A **85**, 415 (2006).
[35]J. Carrasco, B. Santra, K. Kilmeš, and A. Michaelides, Phys. Rev. Lett. **106**, 026101 (2011).
[36]K. Tonigold and A. Groß, J. Comput. Chem. **33**, 695 (2012).
[37]F. F. Wang, G. Jenness, A. A. Al-Saidi, and K. D. Jordan, J. Chem. Phys. **132**, 134303 (2010).
[38]M. Dion, H. Rydberg, E. Schröder, D. C. Langreth, and B. I. Lundqvist, Phys. Rev. Lett. **92**, 246401 (2004).
[39]R. Martínez-Casado, B. Meyer, S. Miret-Artés, F. Traeger, and C. Wöll, J. Phys. Condens. Matter **19**, 305006 (2007).
[40]A. Chizmeshya, M. W. Cole, and E. Zaremba, J. Low Temp. Phys. **110**, 677 (1998).
[41]See supplementary material at http://dx.doi.org/10.1063/1.3698173 for numerical details, additional figures and movies of the dynamical evolution of the helium droplet.
[42]R. Dovesi, V. R. Saunderds, C. Roetti, R. Orlando, C. M. Zicovich-Wilson, F. Pascale, B. Civalleri, K. Doll, N. M. Harrison, I. J. Bush, P. D'Arco, and M. Llunell, *CRYSTAL09 User's Manual* (University of Torino, Torino, 2006).
[43]J. P. Perdew, K. Burke, and M. Ernzerhof, Phys. Rev. Lett. **77**, 3865 (1996).
[44]H. J. Monkhorst and J. D. Pack, Phys. Rev. B **13**, 5188 (1976).
[45]G. Cabailh, X. Torrelles, R. Lindsay, O. Bikondoa, I. Journard, J. Zegenhagen, and G. Thornton, Phys. Rev. B **75**, 241403 (2007).
[46]W. Busayaporn, X. Torrelles, A. Wander, S. Tomić, A. Ernst, B. Montanari, N. M. Harrison, O. Bikondoa, I. Journard, J. Zegenhagen, G. Cabailh, G. Thorston, and R. Lindsay, Phys. Rev. B **81**, 153404 (2010).
[47]M. C. Righi and M. Ferrario, J. Phys.: Condens. Matter **19**, 305008 (2007).
[48]A. Schüller, D. Blauth, J. Seifert, M. Busch, H. Winter, K. Gärtner, R. Wlodarczyk, J. Sauer, and M. Sierka, Surf. Sci. **606**, 161–173 (2012).
[49]U. Garibaldi, A. C. Levi, R. Spadacini, and G. E. Tommei, Surf. Sci. **48**, 649 (1975).
[50]R. Rousseau, H. Khemliche, A. G. Borisov, and P. Roncin, Phys. Rev. Lett. **98**, 016104 (2007).
[51]E. Esbjerg and J. K. Nørskov, Phys. Rev. Lett. **45**, 807 (1980).
[52]G. Benedek, G. Brusdeylings, V. Senz, J. G. Skofronick, J. P. Toennies, F. Traeger, and R. Vollmer, Phys. Rev. B **64**, 125421 (2001).
[53]D. Farias and K. H. Rieder, Rep. Prog. Phys. **61**, 1575 (1998).
[54]H. Onishi and Y. Iwasawa, Surf. Sci. **313**, L783 (1994).
[55]U. Diebold, J. F. Anderson, K. Ng, and D. Vanderbilt, Phys. Rev. Lett. **77**, 1322 (1996).
[56]G. Armand and J. R. Manson, Surf. Sci. **119**, L299 (1982).
[57]G. Wolken, Jr., J. Chem. Phys. **58**, 3047 (1972).
[58]S. Grimme, J. Comput. Chem. **27**, 1787 (2006).
[59]Y. Zhang and W. Yang, Phys. Rev. Lett. **80**, 890 (1998).
[60]G. Kresse and J. Hafner, Phys. Rev. B **47**, 558 (1993).
[61]G. Kresse and J. Furthmüller, Phys. Rev. B **54**, 11169 (1996).
[62]J. Kilmeš, D. R. Bowler, and A. Michaelides, Phys. Rev. B **83**, 195131 (2011).
[63]K. Lee, E. Eamonn, L. Kong, B. I. Lundqvist, and D. C. Langreth, Phys. Rev. B **82**, 081101(R) (2010).
[64]W. Hujo and S. Grimme, Phys. Chem. Chem. Phys. **13**, 13942 (2011).
[65]K. Pernal, R. Podeszwa, K. Patkowski, and K. Szalewicz, Phys. Rev. Lett. **103**, 263201 (2009).
[66]B. Johnson and R. J. Hinde, J. Phys. Chem. A **115**, 7112 (2011).
[67]P. Fowler and J. M. Hustson, Surf. Sci. Lett. **165**, 289 (1986).
[68]V. Dimitrov and S. Sakka, J. Appl. Phys. **79**, 1736 (1996).
[69]G. Benedek, G. Brusdeylins, V. Senz, J. G. Skofronick, J. P. Toennies, F. Traeger, and R. Vollmer, Phys. Rev. B **64**, 125421 (2001).
[70]F. Dalfovo, A. Lastri, L. Pricaupenko, S. Stringari, and J. Treiner, Phys. Rev. B **52**, 1193 (1995).

[71]D. Mateo, M. Pi, and M. Barranco, Phys. Rev. B **81**, 174510 (2010).
[72]A. Ralston and H. S. Wilf, *Mathematical Methods for Digital Computers* (Wiley, New York, 1960).
[73]M. Frigo and S. G. Johnson, Proc. IEEE **93**, 216 (2005).
[74]M. Pi, R. Mayol, A. Hernando, M. Barranco, and F. Ancilotto, J. Chem. Phys. **126**, 244502 (2007).
[75]F. Ancilotto, M. Barranco, F. Caupin, R. Mayol, and M. Pi, Phys. Rev. B **72**, 214522 (2005).
[76]R. A. Aziz and M. J. Slaman, J. Chem. Phys. **94**, 8047 (1991).
[77]L. Verlet, Phys. Rev. **159**, 98 (1967).
[78]H. J. C. Berendsen, J. P. M. Postma, W. F. van Gunsteren, A. DiNola, and J. R. Haak, J. Chem. Phys. **81**, 3684 (1984).